Journal of Power Sources 644 (2025) 237045

Contents lists available at ScienceDirect

Journal of Power Sources

journal homepage: www.elsevier.com/locate/jpowsour

A 25 cm^2 single Si-based solar redox flow battery with aqueous iodine-bromine redox couples

Jungmyung Kim [a], Tasneema Akhtar [b,1], Yanxin Liu [c], Vladimir Smirnov [c], Hwapyong Kim [d], Su-Il In [d], Dong-Heon Han [a,e], Dowon Bae [a,*]

[a] Wolfson School of Mechanical, Electrical and Manufacturing Engineering, Loughborough University, Loughborough, LE11 3TU, UK
[b] Institute of Mechanical, Process and Energy Engineering (IMPEE), School of Engineering and Physical Sciences, Heriot-Watt University, Edinburgh, EH14 4AS, UK
[c] Institute of Energy Materials and Devices (IMD-3) Photovoltaics, Forschungszentrum Jülich, Jülich D-52425, Germany
[d] Department of Energy Science & Engineering, DGIST, Daegu, 42988, Republic of Korea
[e] School of Energy, Materials and Chemical Engineering, Korea University of Technology and Education, Cheonan, 31253, Republic of Korea

HIGHLIGHTS

- The 25 cm^2 Si-based SRFB achieved a solar-to-chemical efficiency (STC) of 9.54 %.
- This system uses Iodide-Bromide redox couples in a neutral pH aqueous electrolyte.
- A 360-hour-long cycle with a maximum SOEE of 3.11 % demonstrated.
- Electrochemical analysis shows high reversibility and stability of the redox couple.

GRAPHICAL ABSTRACT

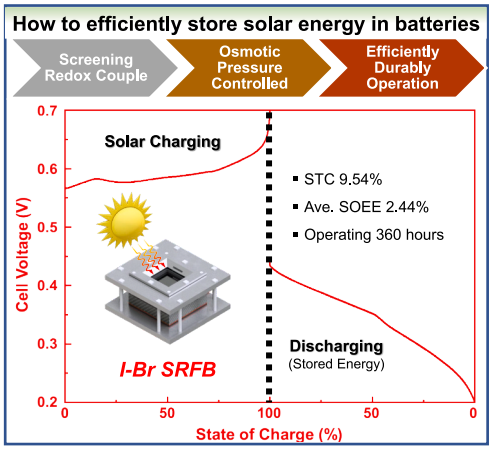

ARTICLE INFO

Keywords:
Solar redox flow battery
Iodine-bromine
Photoelectrochemistry
New redox couple
Aqueous electrolyte

ABSTRACT

Solar redox flow battery (SRFB) technology offers a compelling strategy for the efficient conversion and storage of solar energy, mitigating the intermittency challenges associated with renewable energy sources. This study presents an experimental investigation into the performance of a 25 cm^2 SRFB employing a single-junction silicon photo-device coupled with a neutral pH aqueous iodine-bromine redox couple. The iodine-bromine redox couple was selected through a preliminary screening process, considering its compatibility with the photovoltaic device's current-voltage performance and desirable electrochemical properties. Experimental results demonstrate the successful integration of a 25 cm^2 photoactive-area device with the SRFB system, showcasing efficient solar charging capabilities. The integrated SRFB presented in this study reaches a solar-to-chemical (STC)

* Corresponding author.
E-mail addresses: tasneema_akhtar@outlook.com (T. Akhtar), d.bae@lboro.ac.uk (D. Bae).
[1] T.A. is currently at Verco Advisory Services Ltd.

https://doi.org/10.1016/j.jpowsour.2025.237045
Received 28 January 2025; Received in revised form 26 March 2025; Accepted 10 April 2025
Available online 26 April 2025

conversion efficiency of 9.54 %. Subsequent discharge of the stored chemical energy yielded a maximum solar-to-output electricity efficiency (SOEE) of 3.11 %, with an average efficiency of 2.44 % over a continuous 360-hour cycling period. Furthermore, the electrochemical characterisation of the iodine-bromine redox couple confirmed desirable reversibility and stability. These findings underscore the potential of neutral pH aqueous iodine-bromine redox couples for scalable and sustainable solar energy storage applications, providing valuable insights for the further scale-up of SRFB systems.

1. Introduction

Harvesting energy directly from sunlight is considered one alternative route to a more sustainable energy source compared to power generation reliant on fossil fuels. Simply put, a substantial amount of solar energy, approximately 5,938 times the world's primary energy consumption (6.4×10^{20} J) in 2022, reaches the Earth's surface. However, the intermittent nature of solar radiation challenges grid stability and transmission/distribution efficiency.

In response to these challenges, significant research efforts have been directed towards photoelectrochemistry (PEC) technologies for direct solar energy conversion [1–4]. Notably, recent attention has focused on solar redox flow cells [5], or batteries (SRFCs or SRFBs), which offer the advantage of electrochemical solar energy storage coupled with facile reaction kinetics and generation of electricity *via* reversible reactions [6–11]. SRFBs can be broadly categorised into two major configurations [12]. The first is the monolithic integration of the PEC device and redox flow battery (RFB), establishing a direct device/liquid interface between the semiconductor photoelectrode (PE) and the redox electrolyte. The coupled solar batteries enable direct solar energy storage *via* photo-coupled ion transfer (PCIT); however, charge recombination and energy level misalignment remain critical performance-limiting factors. Recent advancements, including covalent organic framework (COF)-based architectures and molecular photoelectrochemical materials, have yielded notable enhancements in solar-to-electrochemical energy storage efficiency [13–15]. The second approach employs physical integration (i.e., mechanically stacked up) of photo-devices and flow cells [16,17]. In this integration, electrons and heat transfer occur across the solid/solid interface of the physically stacked assembly of photovoltaic (PV) devices and RFB cells, but ions are transferred between each electrode. Effective SRFB design necessitates careful selection of redox couples, considering both the redox potential of the redox couple and the operating voltage of the semiconductor-based photoelectrode. While maintaining RFB's capacity and power decoupling advantage, SRFB additionally has the potential to mitigate the photovoltaic device's overheating under prolonged light exposure through heat transfer to the liquid flow [7,18].

The vanadium redox couple has been extensively investigated as the most suitable for commercial RFB [19–22]. In addition to their well-established electrochemical stability and scalability, recent research has underscored the techno-economic benefits of vanadium redox flow batteries (VRFBs) when integrated into solar energy systems. Zheng et al. demonstrated that VRFB can achieve a high round-trip efficiency (RTE) exceeding 78 % while also offering a cost-effective solution with a levelised cost of energy (LCOE) lower than hydrogen-based storage alternatives, highlighting their suitability for large-scale solar energy storage applications [23]. While some studies have explored all-vanadium systems for SRFB applications [24,25], challenges remain. These include the toxicity of the vanadium in strongly acidic electrolytes (e.g., sulfuric acid or hydrochloric acid), its limited operating temperature range (10–45 °C [26]) due to the precipitation formation problem of VO_2^+ ions, and potential scarcity impacting its commercial viability [27]. The chosen redox couples for SRFB must be compatible with the performance curve of PE and the operating potential between the redox couple to ensure the system's stable charging performance. By matching the operating voltage range of the charging PE in the SRFB and the cell voltage (V_{cell}) of the system, high states of charge (SOC) can be achieved without requiring additional bias [28]. Notably, the SOC-dependent shift of the V_{cell} also should be considered [29]. For instance, Wedege et al. demonstrated 95 % SOC using a c-Si photocathode with a photovoltage exceeding the standard V_{cell} by ca. 30 % [28]. In a recent study by Wang et al. [30], a Fe–Br-based solar-rechargeable redox flow battery (SRFB) was fabricated using 3D printing technology, utilising Mo-$BiVO_4$ and polyterthiophene (PTTh) dual photoelectrodes to achieve efficient solar energy conversion and storage. In addition, the 3D-printed system demonstrated significantly improved discharge capacity and initial discharge voltage compared to H-type cells, achieving approximately 10-fold higher discharge capacity, thereby proving its efficiency and stability. However, SRFB is still at an early research stage based on trial-and-error screening of redox chemicals [31,32]. Given that typical flow cells operate under higher cell voltage conditions [33] than PV devices, careful preselection of compatible redox couples is crucial for effective solar-driven RFB charging. This compatibility often necessitates more complex device architectures, such as heterogeneous multi-junction or interconnected solar charging devices [34–37] (see Fig. 1).

In this study, we present a zero-gap SRFB system (illustrated in Figs. 1 and S1) incorporating a relatively large active area of 25 cm^2 silicon heterojunction (SHJ) photovoltaic device (Fig. 2), representing one of the largest SRFB active areas reported to date [7,11]. We focus on the experimental evaluation of a carefully selected redox couple chosen for its compatibility with the SHJ device's operating voltage, which is responsible for charging the SRFB system. We also experimentally evaluated a competitive osmotically balanced neutral pH aqueous iodine/bromine redox couples combination, which, to the best of our knowledge, has not been previously explored in solar-power electrochemical energy storage applications. The outcomes of this study offer valuable insights and practical guidelines for the engineering scale-up required for further practical application of this solar-rechargeable RFB technology.

2. Experimental

2.1. Electrolyte preparation

The electrolyte for electrochemical evaluation was prepared by

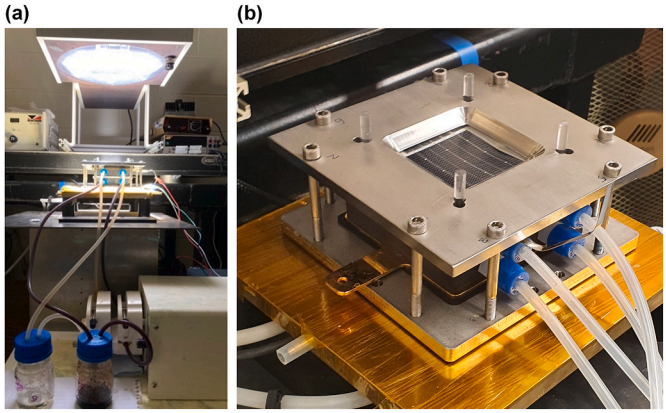

Fig. 1. Photo of the (a) whole experimental SRFB setup integrated with a pumping system and electrolyte tanks and (b) diagonal view of SRFB with 25 cm^2 active area.

adding 1 M KCl (potassium chloride, Thermo scientific, 99 %) as a supporting electrolyte. 1 M KBr (potassium bromide, Alfa Aesar, 99 %) was used as the active ion in the anolyte preparation. 1 M I_2 (Iodine, Thermo scientific, 99 %) and 1 M KI (potassium iodide, Sigma-Aldrich, 99 %) were used as active ions in catholyte preparation. The electrolyte used in the charge/discharge experiments using a single cell was an electrolyte whose osmotic pressure was adjusted according to the following equilibrium equation (Eq. (1)) [38]:

$$\Pi = icRT \quad (1)$$

where Π is the osmotic pressure (kPa) dependent on ionic strength, i is the van't Hoff factor (−), c is the concentration (mol L^{-1}), and R is the universal gas constant (8.314 m^3 Pa K^{-1} mol^{-1}). In our study, the concentration of the negative electrolyte was controlled based on the positive electrolyte.

2.2. Electrolyte analysis

The fresh electrolytes were measured using a pH meter, and the bromine and iodine electrolytes were 6.618 ± 0.011 and 7.830 ± 0.008, respectively. The electrochemical performance analysis of the osmotically balanced neutral pH aqueous iodine/bromine electrolytes introduced in this study to charge the RFB system using a photovoltaic device was measured using an electrochemical workstation for potentiostat/galvanostat (Biologic - SP-50e). Each electrolyte sample used in standard three-electrode cyclic voltammetry (CV) had completed one charge/discharge cycle. All three electrodes were made of ALS products: the reference electrode (ASL, RE-1B 012167) was Ag/AgCl with saturated KCl solution, the counter electrode (ASL, 012961) was 23 cm long spiral Pt, and the working electrode (ASL, 002012) was glassy carbon with a diameter of 3 mm.

2.3. Solar-redox flow battery cell assembly

The Silicon Heterojunction (SHJ) solar cells were fabricated using M2-size n-type Czochralski (CZ) crystalline silicon as-cut wafers with resistivity of 1–5 Ωcm and a thickness of 130 μm. The wafers were firstly chemically etched to remove saw damage and then textured in an alkaline solution to obtain random pyramids (Fig. S2) on both sides. Intrinsic and doped thin film silicon layers were deposited in an AK 1000 plasma-enhanced chemical vapor deposition (PECVD) tool from Meyer Burger. Around 80 nm of indium tin oxide (ITO) layers were sputtered from a 3 % Sn-doped In_2O_3 target onto both sides of the wafers with a direct current mode. The cells (size 25 cm^2) were cut out of the wafer with a laser and characterised under simulated sun irradiation (AM1.5G). Encapsulated using a glass/thermoplastic polyolefin (TPO)/back sheet was performed. Additional details can be found in Fig. S1 and references [39,40].

The light illumination used for the PV cell testing and charging process of SRFB is ABET Technologies' 11044A model (AAA grade) containing a 150W DC Xe arc lamp. The simulated sunlight used for charging represents 1 solar equivalent lighting (i.e., 1 sun) at AM 1.5G spectral match A grade (100 mW cm^{-2}).

The SRFB cell used in the experiments is joined to a stainless-steel outer frame (160 mm × 160 mm x 8 mm) with a window for a photovoltaic device measuring 50 mm × 50 mm (25 cm^2 active area) on one side. To secure all cell layers and prevent slipping, four holes (6.4 mm) for guide bars were added to each corner of the cutout window. Two rubber spacers with size 110 mm × 110 mm x 2.5 mm and a window size of 65 mm × 65 mm were applied. The window cutouts in the rubber surface are larger than the PV charging device's active area, preventing shading and the application of direct pressure. A rubber gasket was chosen to avoid unintentional conduction of electricity between cell layers. The anode electrode of the PV device is directly connected to the bipolar plate of the RFB cell, and the cathode electrode sticks out and is connected to a potentiostat. The RFB cell used in our study has the same layout as the typical configuration of a flow battery [11,20]. Charge/-discharge cycling was performed within a 0.2–1.0 V potential window. During the constant current charge/discharge process, a constant current of 100 mA was applied, while during the solar charging regime, the condition of charging through the solar cell, the rated current changes according to the voltage. This is due to the characteristics of the solar cell's I-V curve (refer to Fig. 7 for details). The electrolytes were stored in sealed containers of 500 mL each and were supplied to the active area of the cell at a flow rate of 50 mL min^{-1}. The 50 mm × 50 mm graphite felt (SGL carbon, SIGRACELL GFD 4.65 EA) electrodes and cation exchange membrane (FuelCell Store, Fumasep FKS-30) were untreated and used after immersion in 1 M KCl solution for 1 h.

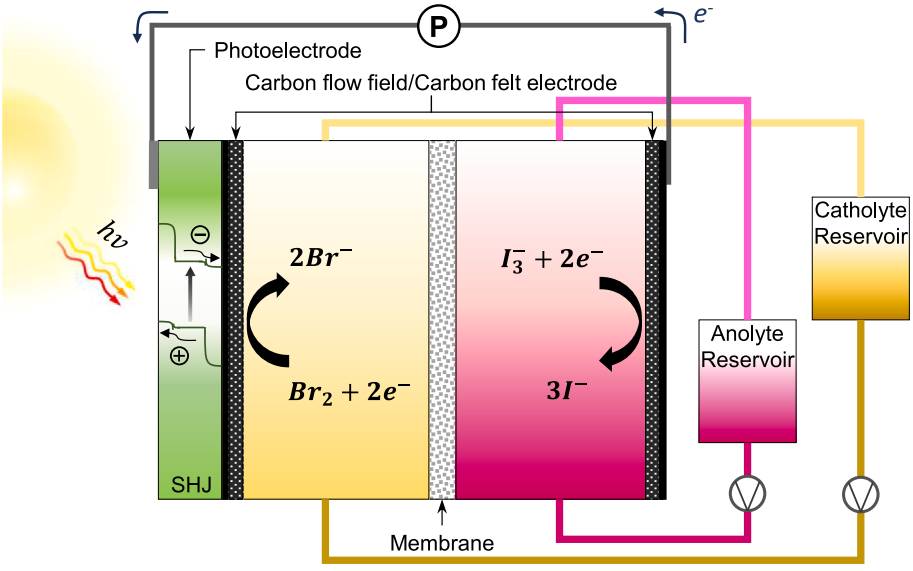

Fig. 2. Schematic diagram of a redox flow battery (RFB) cell integrated with silicon solar cells of the solar redox flow battery (SRFB) tested in this work. Note that the illustration is not to scale, and the space between the charge collectors and the membrane is filled with the carbon felt (i.e., zero-gap condition; see also Fig. S1). (For interpretation of the references to colour in this figure legend, the reader is referred to the Web version of this article.)

3. Results and discussion

The results of the screening metrics for selecting redox pairs are summarised in Fig. 3. The figure presents a matrix, in total, for 36 redox couples, with cations and anions ordered by their standard potentials (E_0) in descending order. The number at the intersection of each ion represents the theoretical redox potential of the redox couple. The solubility is determined by the less soluble of the two redox couples, and the pH range was chosen to be compatible with the redox reaction of each redox couple. A critical criterion for the screening matrix is identifying new redox couple combinations, matching the operating voltage and photovoltage maximum of the SHJ solar-charging device (open circuit voltage (V_{oc}) of ca. 0.7 V with a maximum power point (P_{max}) below 0.6 V). This ensures efficient charging of the RFB cell by the single-junction photovoltaic device. Based on this criterion, the I^-/I_3^- and Br^-/Br_2 redox couples were prioritised. A critical criterion for the screening matrix is identifying new redox couple combinations that align with the operating voltage and maximum photovoltage of the SHJ solar-charging device. This ensures the efficient charging of the RFB cell by the single-junction photovoltaic device. Based on this criterion, the I^-/I_3^- and Br^-/Br_2 redox couples were prioritised. Beyond voltage compatibility, additional factors such as solubility and long-term stability were also considered in the selection process [41]. While some alternative redox couples exhibited comparable redox potentials (e.g., 0.56 V and 0.60 V), their applicability was constrained by lower solubility, which could restrict the achievable energy density. In contrast, both the I^-/I_3^- and Br^-/Br_2 couples exhibit high solubility in aqueous electrolytes, which allows for higher active species concentrations and improved capacity. Moreover, cost analysis favoured the iodine-bromine system due to the relative abundance and accessibility of these halogen species compared with alternative transition metal-based redox couples. Notably, halogen-based RFB systems have been reported to achieve system-level costs in the range of approximately 85–148 USD kWh^{-1}, which is substantially lower than the 300–600 USD kWh^{-1} typically associated with conventional VRFB systems [42]. Accordingly, while voltage compatibility was established as the primary selection criterion, additional considerations of solubility, cost-effectiveness, and long-term stability further supported the selection of the iodine–bromine redox couple over other candidates.

As shown in Fig. 4, the I-Br redox couple combination can exhibit a standard cell voltage (potential differences between the I^-/I_3^- and Br^-/Br_2 redox couples) of 0.60 V, consistent with the value from the literature-driven screening matrix in Fig. 3. These measurements were taken at room temperature and a scan rate of 100 mV s^{-1}. The mechanisms of Br^- oxidation and Br_2 reduction that occur in the anode active area of the RFB cell have been detailed by Brent et al. and further substantiated in subsequent research [43]. Furthermore, the high vapor pressure characteristic of bromine makes it challenging to maintain the concentration of active ions during long-term operation, but this can be improved by introducing a bromine capturing agent (BCA) [44,45].

In Fig. 5a and b presents the Randles-Sevcik plot derived from the CVs of selected redox couples [46]. In general, the redox reaction of Br^-

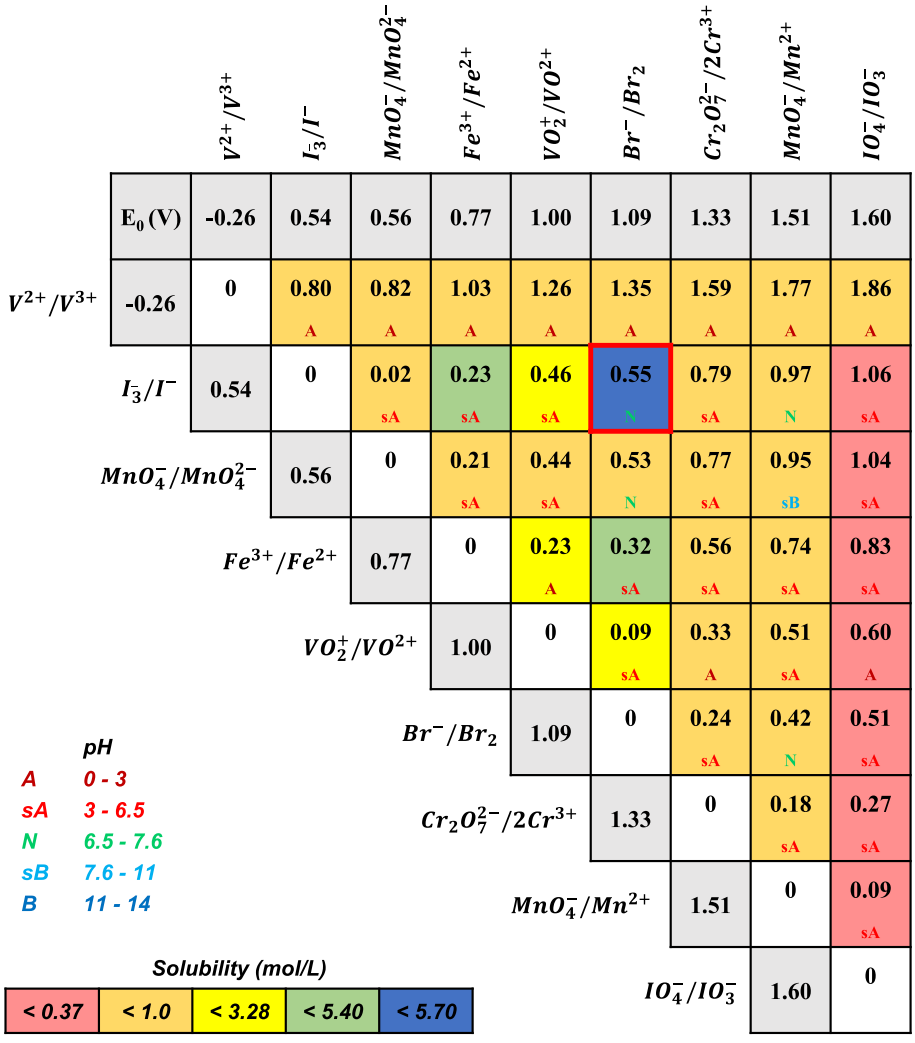

Fig. 3. Screening metrics for selecting redox couples for SRFB systems can identify standard potential, redox potential, solubility, and pH range.

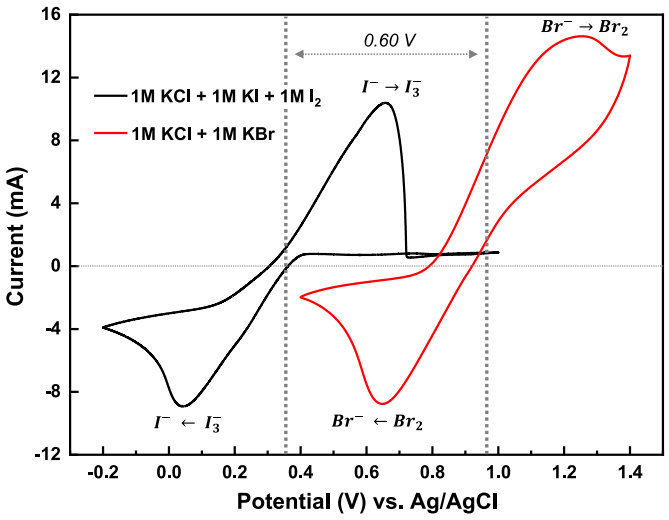

Fig. 4. Cyclic voltammetry for electrochemical characterisation of redox couple aqueous solutions.

ions, especially the reduction reaction, is irreversible at carbon electrodes [43], particularly under high current density conditions, the observed linear relationship between peak current and the square root of scan rate (60 mV s^{-1}) suggests that the mass transfer is primarily diffusion-controlled within the employed scan rates. Therefore, the irreversible properties due to the high vapor pressure of Br [43], as reported in several studies, are not considered to have occurred in our experimental conditions. As shown, iodine (Fig. 5c) exhibits a reversible CV curve compared to the redox reaction of bromine (Fig. 5d). In addition, the I^-/I_3^- redox conversion follows a well-defined electrochemical process at the electrode surface ($3I^- \rightarrow I_3^- + 2e^-$ and $I_3^- + 2e^- \rightarrow 3I^-$), while a chemical equilibrium ($I_2 + I^- \leftrightarrow I_3^-$) occurs simultaneously in the bulk solution. This mixed mechanism is characteristic of iodine-based systems and is confirmed by both CV and charge/discharge profiles, demonstrating Butler-Volmer kinetics and stable reversibility under our experimental conditions. More detailed analyses can be found in Fig. S3 and SI Note 1. Additionally, the excellent reversibility of the Br/I couple is evident in the charge/discharge results for the SRFB system.

The charge/discharge behaviour of the SRFB cell with selected redox couples is shown in Fig. 6. The figure shows the solar charging and GCD (galvanostatic charge-discharge) discharge curves separately (black and red, respectively) obtained under 100 mA constant current mode. To minimise polarisation effects, a 10-min open-circuit rest period (no-load operation) between charge and discharge cycles was implemented with a charge voltage limit of 0.7 V. The figure also includes photographs illustrating the colour changes of each electrolyte under RFB mode as a function of SOC change. The bromine electrolyte is initially colourless and transparent, but its transparency decreases (turns brown) in proportion to the SOC during the charge/discharge process, corresponding to the oxidation of Br^- to Br_2. This colour change reflects the increasing concentration of tribromide species. The iodide electrolyte is generally colourless in aqueous solution. However, the concentration of molecular iodine is dominant, and the electrolyte used in this work is dark yellow-brown under standard operating conditions. In the overcharged state, the iodine ions in the electrolyte form a higher oxidation state and become transparent. The transparent iodine electrolyte can be seen in Fig. S4. Charging and discharging took approximately 14 and 13 h, respectively, and the electrolyte level (500 mL each) in each electrolyte storage tank remained constant during repeated experiments, indicating no significant electrolyte loss due to evaporation or other processes. These standard potential results were validated with our SRFB system. Specifically, the power produced by a silicon PV device was successfully stored (charged) in an RFB cell.

The linear sweep voltammetry (LSV) curves for the RFB mode in Fig. 7a were measured immediately following full discharging and charging, after a dwell period under open-circuit conditions (V_{OC} of 0.336 V and 0.531 V at SOC 0 % and 100 %, respectively). The photocurrent increases by approximately 2.7 times at the given bias as the SOC increased. This enhancement is attributed to a shift in the

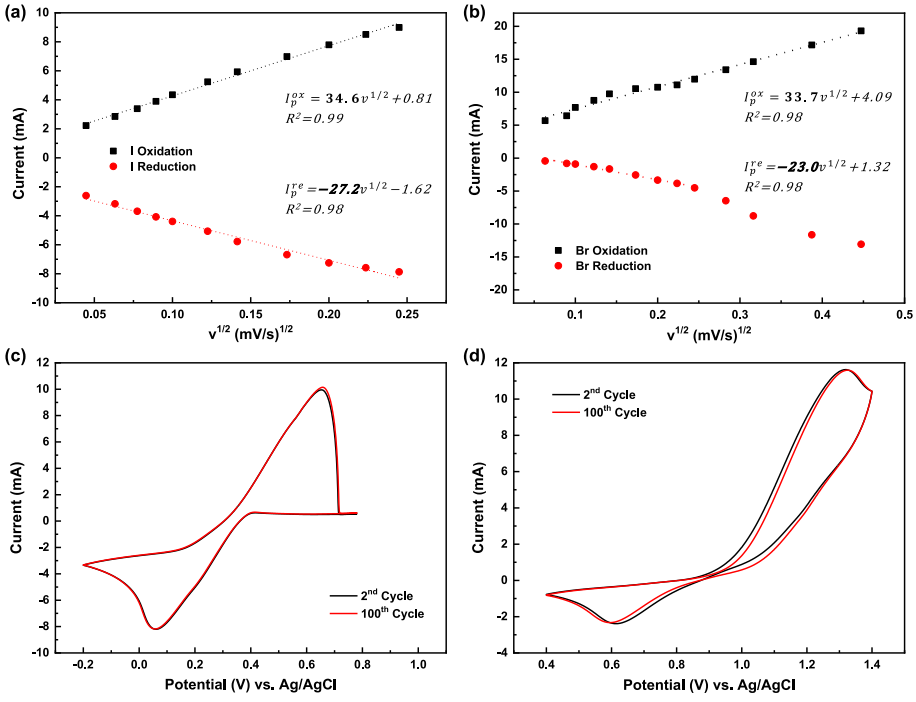

Fig. 5. Linear relationship between oxidation/reduction peak current and square root of scan rate ($v^{1/2}$) for (a) I^-/I_3^- and (b) Br^-/Br_2 electrolytes. In addition, CV curves of 100 consecutive cycles for (c) I^-/I_3^- and (d) Br^-/Br_2 were measured at a constant scan rate (60 mV s^{-1}). The electrolyte used in the measurements was all 100 % SOC, with a molar concentration of 1 M KBr and 1 M KI and 1 M I_2.

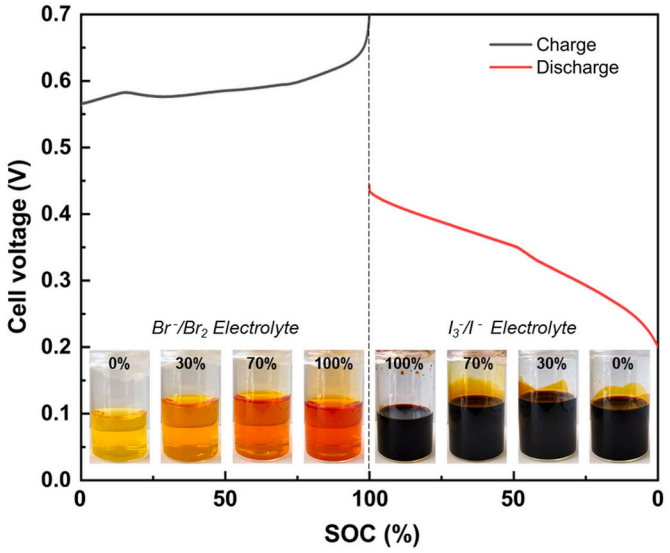

Fig. 6. Solar charging and GCD discharge curves (black and red, respectively) and colour changes of each electrolyte under RFB mode as it changes oxidation state. (For interpretation of the references to colour in this figure legend, the reader is referred to the Web version of this article.)

photocurrent onset potential with increasing SOC.

Fig. 7b presents the overlaid IV curves of the PV regime (i.e., dry condition) only (dark) and SRFB system. The mechanically stacked PV device served as the power source for charging the SRFB. As expected, it is anticipated that employing a high-efficiency photo-device could further enhance the charging rate of the SRFB and consequently reduce its charging time. Under the same unbiased two-electrode condition, both the PV device and SRFB charging modes exhibited a photocurrent of approximately 300 mA (ca. 12 mA cm^{-2}). A notable aspect of the LSV curve of the SRFB is that the current begins to decrease as the voltage exceeds 0.4 V. This I-V characteristic of photo-device at low current region can actually be an advantage for RFB, as it can reduce the concentration overvoltage at high SOC. Furthermore, the change in slope observed in the current reduction region of the PV cell and the SRFB indicates an increased series resistance in the SRFB operation regime. This increase is attributed to the increased contact resistance resulting from the mechanical contact between the photovoltaic device and the bipolar plate of the SRFB, an important factor that should be considered for future system scaling and integration.

Fig. 8a presents the charging behaviour of the SRFB system with various electrolyte conditions and cycling numbers under simulated solar illumination. The black solid line represents the results of the 3rd galvanostatic charging of pristine electrolyte prepared at a 1 M concentration, while the black dotted line indicates the 10th charge. The polarisation effect increases most dramatically with the number of cycles, likely attributed to electrolyte crossover through the membrane [38], resulting in different electrolyte volumes in the two electrolyte reservoirs. During cycling tests with pristine electrolyte conditions, a decrease in the anode electrolyte storage capacity was observed. This crossover increases polarisation losses caused by the concentration difference between the anode and cathode electrolytes [38].

To mitigate this crossover issue, we introduced an osmotic pressure-controlled electrolyte solution. The red line in Fig. 8a shows the result of charging with a controlled osmotic pressure (COP) electrolyte. To apply the COP, 1 M KBr and 1 M KCl electrolytes were set as references. This was chosen due to the solubility limit of aqueous solutions. Using Eq. (1) in Section 2.2, the concentrations of KI and I_2 were calculated to be 0.667 M. The concentrations of KI and I_2 used in this study were chosen to be 1:1. And the concentration of KCl was the same as that of the Br electrolyte (1 M). While this approach resulted in a slightly lower initial energy capacity compared to the pristine electrolyte due to the adjusted ionic strength of the I^-/I_3^- couple, it significantly improved capacity retention by suppressing water crossover (Fig. 8b). Additionally, the results of solar-charging with an electrolyte adjusted for osmotic pressure balance are shown in blue lines. The SRFB system exhibited the same electrochemical charging characteristics seen in the constant current charging process (red line) of an RFB charging/discharging regime, demonstrating the compatibility of the COP electrolyte with the solar-charging regime. The volume of COP electrolyte remained consistent with the initial electrolyte volume even after the end of the cycling experiment, implying the mass transport through the membrane, i.e., crossover, was significantly reduced with the COP electrolyte compared to the pristine electrolyte. Furthermore, as can be seen from the LSV curve of the PV device, the relatively low charging current at charging conditions above 80 % SOC provides deep charging and reduces the risk of side reactions.

During the charging process, as the SOC of the cell approaches 100 %, the charging current driven by the photovoltaic device to the cell decreases, resulting in relatively improved reversibility (discharge capacity retention rate) due to the lowered contribution from the ohmic overpotential. Furthermore, the voltage plateau observed above 90 % SOC during the SRFB charging process is attributed to the photovoltage limit, with the SRFB voltage remaining below the 0.7 V limit due to the PV device's I-V characteristics. However, the rapid voltage increase (i.e., concentration overpotential) that occurs from approximately 80 % SOC is a typical performance characteristic of RFBs. This is due to the current level supplied by the photo-device relative to the increasing polarisation loss caused by mass transfer limitations and depletion of active ions.

To quantitatively assess our SRFB system performance, the solar-to-chemical (STC) conversion efficiency and solar-to-output electricity efficiency (SOEE) are expressed as follows [47]:

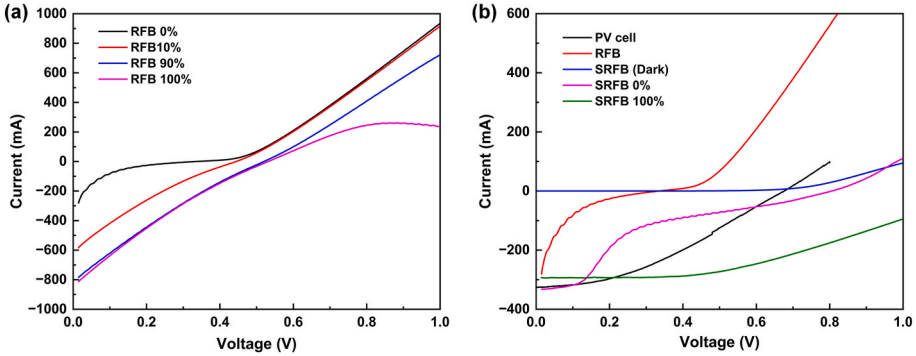

Fig. 7. Current-voltage (J–V) curves recorded (a) RFB and (b) with and without light for various cell conditions using a two-electrode setup. SOC was classified through OCV measurement after each stage of charging/discharging.

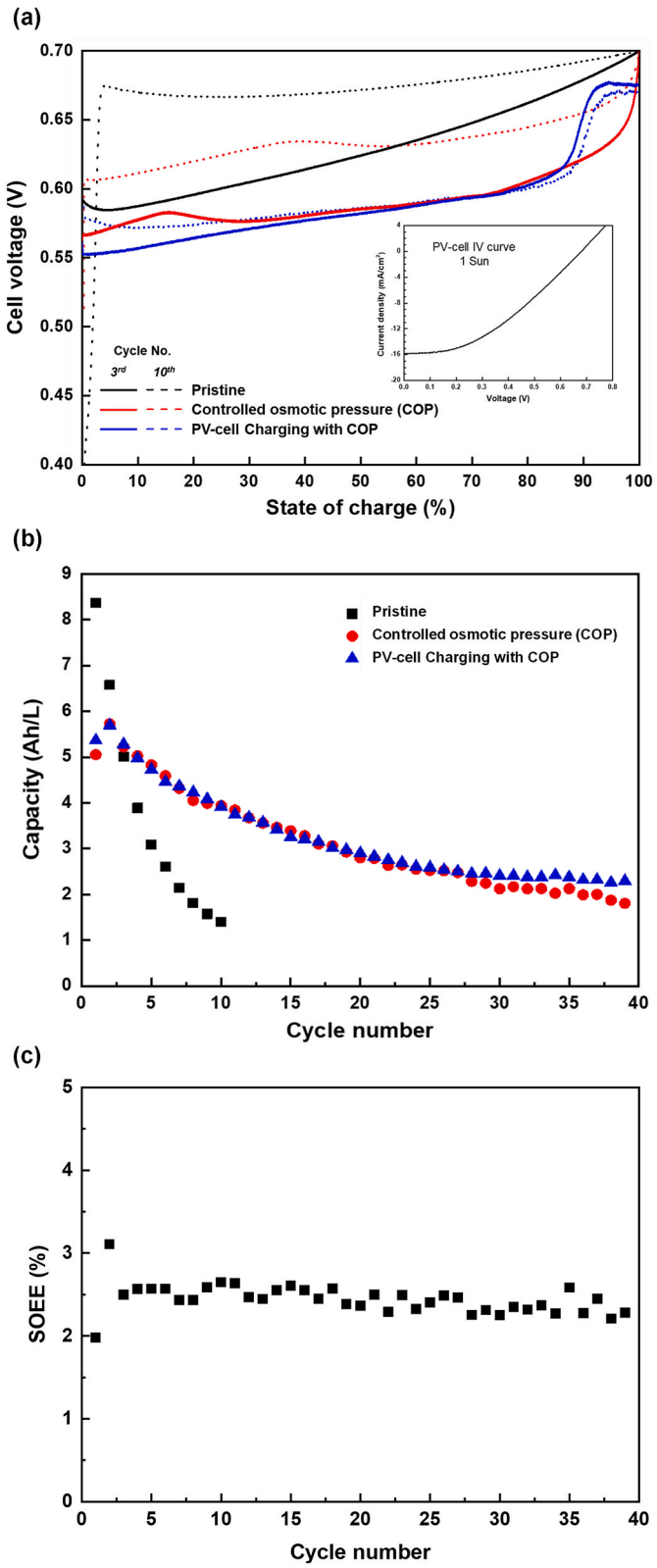

Fig. 8. (a) Comparison of cell voltage according to the charge state of SRFB with 25 cm^2 active area, (b) discharge capacity according to charge/discharge cycle and (c) SOEE of converting input solar energy into output power of SRFB.

$$STC(\%) = \frac{j_{op} E_{redox}}{P_{input}} \tag{2}$$

$$SOEE(\%) = \frac{E_{discharge}}{E_{illumination}} = \frac{\int I_{dis} V_{dis} dt}{\int SA dt} \tag{3}$$

where j_{op} is the operating photocurrent density or measured current density at zero bias voltage under the two-electrode conditions, E_{redox} is the redox potential difference, P_{input} is the power of solar radiation, I_{dis} is the output current, V_{dis} is the output voltage, S is the incident solar power density, and A is the area of the photoelectrode. The STC calculated using Eq. (2) is 9.54 %, while the SOEE calculated using Eq. (3) remains relatively constant at a maximum of 3.11 % and an average of 2.44 % for the entire cycle (Fig. 8c). STC represents the instantaneous efficiency of converting solar energy into chemical energy during charging, while SOEE reflects the cumulative efficiency across the entire charging (i.e., solar storage) and discharging processes. The disparity between the STC of 9.54 % and the SOEE of 2.44–3.11 % is attributed to the energy losses inherent in the system coupled with the RFB. These losses encompass the factors, including charge transfer overvoltage, shunt current, self-discharge, and voltage inefficiency during discharge. Matching the operating voltage ranges of photovoltaic devices and RFB cells is the most challenging task in SRFBs when selecting redox couples for the maximisation of STC and SOEE. So, it is noteworthy that our SRFB system has been successfully cycled for over 360 hours.

As seen in Fig. 8a, it is necessary to apply a photovoltaic device with improved photovoltage characteristics to ensure that the redox reaction occurs over a wide voltage range. Based on Eq (3), SOEE could be further improved by selecting redox couples with a potential window that better aligns with the PV device's operating curve. While the silicon-based PV devices introduced so far are readily available and inexpensive, their relatively low voltage output and the narrow potential window of the redox couples that meet this voltage condition constrain SOEE improvement. Furthermore, the SRFB device, with its large active area (25 cm^2), may have experienced unintended electrolyte leakage or stagnation due to its large cell size. As evidenced by the contact resistance observed in Fig. 7b (i.e., high series resistance represented by a moderate slope near open-circuit voltage), efforts to reduce the series resistance of the photo-device are also necessary. In addition, the neutral pH electrolyte gradually becomes acidic as it goes through the charge and discharge process. The following are the pH values measured after the 10th charge and discharge. Under the condition of 0 % SOC, the bromine electrolyte was 1.217 ± 0.014, and the iodine electrolyte was 4.820 ± 0.005. Under the condition of 100 % SOC, the bromine electrolyte was 1.092 ± 0, and the iodine electrolyte was 5.309 ± 0.009. The pH difference that increases with the cycle is because H^+ accumulates to balance the charge for the ions that have moved through the cation membrane [48]. Capacity retention can be further improved by modifying the membrane or by using a system that takes pH into account.

Despite these limitations, this work demonstrates a long-period and relatively high STC efficiency single-junction photo-device-based SRFB in the largest reported area (25 cm^2). However, considering the current solar cell size, there is still room for further improvement. Additionally, achieving enhanced SOEE relies on minimising the series resistance and the shunt currents of the photo-device through improved cell architecture. Despite these challenges, this study demonstrates the feasibility of large-area (25 cm^2) SRFBs with stable long-term operation, providing a critical step towards scaling up economically viable systems (<USD 100 per semiconductor [49]) with uniform mass transfer performance [50].

4. Conclusions

This work demonstrates a 25 cm^2 zero-gap solar-rechargeable redox flow battery, representing one of the largest areas among the single-junction photo-device-based SRFB reported to date. The integrated

system achieved an STC conversion efficiency of 9.54 % and a peak SOEE of approximately 3.11 % during the 39 cycles (total 360-hour operating time) demonstration. This 360-hour total cycle is the longest operation among the single-cell-based SRFB systems published so far. Our findings contribute to advancing solar energy harvesting technology and provide insights for scalable engineering for practical SRFB applications.

A rigorous redox couple screening process was conducted, addressing several key aspects: i) redox potential, ii) operating voltage range, and iii) solubility to maximise the compatibility between the photovoltaic device and the electrolyte system. The chosen iodine-bromine redox couple effectively matched the operating characteristics of the silicon photovoltaic device. Experimental results confirmed the successful integration of a silicon photovoltaic device with an iodine-bromine RFB system, showcasing efficient and unbiased solar charging capabilities. The aligned I-V curves of the PV cell (dry condition) and SRFB regime minimised the concentration overpotential of electrolytes and ensured stable operation within the desired potential range. Moreover, our investigation into the electrochemical properties of the iodine-bromine redox couple revealed its favourable reversibility and stability, as evidenced by cyclic voltammetry and charge/discharge experiments. The use of osmotically controlled electrolyte solutions further enhanced the cycle reversibility and discharge capacity retention rate by mitigating concentration gradients between the anolyte and catholyte. Although the high vapor pressure of bromine presents a potential limitation for long-term operation, ongoing research on bromine-capturing agents (BCAs) may provide an effective mitigation strategy. Furthermore, implementing controlling strategies that limit deep charge/discharge cycles may help maintain bromine concentration in the electrolyte.

Overall, this study highlights the potential of neutral pH aqueous iodine-bromine redox couples for efficient solar energy storage using a silicon-based SRFB system. Considering the dimensions of commercially available crystalline silicon photovoltaic devices, we anticipate that future large-scale SRFB systems will probably consist of interconnected multiple individual modules, each with an active area in the range of 200~400 cm^2.

CRediT authorship contribution statement

Jungmyung Kim: Writing – review & editing, Writing – original draft, Visualization, Investigation, Formal analysis, Data curation. **Tasneema Akhtar:** Investigation, Data curation. **Yanxin Liu:** Writing – review & editing, Investigation, Conceptualization. **Vladimir Smirnov:** Writing – review & editing, Investigation. **Hwapyong Kim:** Writing – review & editing, Investigation. **Su-Il In:** Writing – review & editing. **Dong-Heon Han:** Data curation, Formal analysis. **Dowon Bae:** Writing – review & editing, Visualization, Supervision, Methodology, Investigation, Funding acquisition, Conceptualization.

Declaration of competing interest

The authors declare the following financial interests/personal relationships which may be considered as potential competing interests.

Dowon Bae reports financial support was provided by Engineering and Physical Sciences Research Council. Jungmyung Kim reports financial support was provided by Engineering and Physical Sciences Research Council. Dowon Bae reports financial support was provided by British Council. Jungmyung Kim reports financial support was provided by British Council. Hwapyong Kim reports financial support was provided by National Research Foundation of Korea. Su-Il In reports financial support was provided by National Research Foundation of Korea. Vladimir Smirnov reports a relationship with Research Centre Jülich that includes: employment. Yanxin Liu reports a relationship with Research Centre Jülich that includes: employment. If there are other authors, they declare that they have no known competing financial interests or personal relationships that could have appeared to influence the work reported in this paper.

Acknowledgement

This work was supported by the British Council (Reconnect Programme) and the Engineering and Physical Sciences Research Council of the UKRI (EPSRC; grant no. EP/X015920/2). H.K and S.I. also acknowledge the National Research Foundation of Korea (NRF; grant no. 2021R1A2C2009459). D.H. acknowledges the BK21 FOUR Project of the National Research Foundation of Korea under the Ministry of Education. We thank A. Lambertz and K. Ding (FZ Jülich) for their contributions to the development of photovoltaic structures. We also thank Scott Differ (Heriot-Watt University) for his contribution to SRFB frame and gasket designs.

Appendix A. Supplementary data

Supplementary data to this article can be found online at https://doi.org/10.1016/j.jpowsour.2025.237045.

Data availability

Data will be made available on request.

References

[1] G. Kim, M. Oh, Y. Park, Solar-rechargeable battery based on photoelectrochemical water oxidation: solar water battery, Sci. Rep. 6 (2016) 1–9, https://doi.org/10.1038/srep33400.

[2] A.J. Kaufman, A.C. Nielander, G.J. Meyer, S. Maldonado, S. Ardo, S.W. Boettcher, Absolute band-edge energies are over-emphasized in the design of photoelectrochemical materials, Nat. Catal. 7 (2024) 615–623, https://doi.org/10.1038/s41929-024-01161-0.

[3] A. Khampuanbut, S. Kheawhom, W. Kao-ian, W. Limphirat, H. Uyama, P. Pattananuwat, Unveiling the potential of a g-C_3N_4/BiOBr/$Bi_2O_2CO_3$ ternary heterojunction photocatalyst for rechargeable zinc-air battery: visible-Light-Driven photo-assisted charging for bifunctional ORR and OER at the air cathode, J. Power Sources 612 (2024) 234795, https://doi.org/10.1016/J.JPOWSOUR.2024.234795.

[4] N. Khan, G. Burashev, A. Kadylbekova, T.Sh Atabaev, Z. Bakenov, F. Sultanov, A. Mentbayeva, B. Tatykayev, Sustainable scalable solid-state synthesis of highly efficient synergetic 2D/0D micro/nanostructured g-C_3N_4/CdS photocatalysts for hydrogen production and water purification, Sustain. Mater. Technol. 41 (2024) e01063, https://doi.org/10.1016/j.susmat.2024.e01063.

[5] P. Lu, P. Leung, H. Su, W. Yang, Q. Xu, Materials, performance, and system design for integrated solar flow batteries – a mini review, Appl. Energy 282 (2021) 116210, https://doi.org/10.1016/J.APENERGY.2020.116210.

[6] D. Santander, S. Whitley, J. Kim, D. Bae, Analysis of temperature distribution in PV-integrated electrochemical flow cells, Materials Futures 2 (2023) 045103, https://doi.org/10.1088/2752-5724/acf32e.

[7] S. Whitley, D. Bae, Perspective—insights into solar-rechargeable redox flow cell design: a practical perspective for lab-scale experiments, J. Electrochem. Soc. 168 (2021) 120517, https://doi.org/10.1149/1945-7111/ac3ab3.

[8] B.K. Durant, Y. She, P. Wang, T. Kraus, B.A. Parkinson, Solar charged redox flow battery: a tandem photoelectrochemical approach, J. Electrochem. Soc. 166 (2019) H3001–H3008, https://doi.org/10.1149/2.0011905JES.

[9] W. Li, J. Zheng, B. Hu, H.C. Fu, M. Hu, A. Veyssal, Y. Zhao, J.H. He, T.L. Liu, A. Ho-Baillie, S. Jin, High-performance solar flow battery powered by a perovskite/silicon tandem solar cell, Nat. Mater. 19 (2020) 1326–1331, https://doi.org/10.1038/s41563-020-0720-x.

[10] Y. Zhou, S. Zhang, Y. Ding, L. Zhang, C. Zhang, X. Zhang, Y. Zhao, G. Yu, Efficient solar energy harvesting and storage through a robust photocatalyst driving reversible redox reactions, Adv. Mater. 30 (2018) 1802294, https://doi.org/10.1002/ADMA.201802294.

[11] T. da Silva Lopes, P. Dias, R. Monteiro, A. Vilanova, D. Ivanou, A. Mendes, A 25 cm^2 solar redox flow cell: facing the engineering challenges of upscaling, Adv. Energy Mater. 12 (2022) 2102893, https://doi.org/10.1002/aenm.202102893.

[12] W. Li, S. Jin, Design principles and developments of integrated solar flow batteries, Acc. Chem. Res. 53 (2020) 2611–2621, https://doi.org/10.1021/acs.accounts.0c00373.

[13] X. Zhang, L. Jiao, Y. Wang, Molecular photoelectrochemical energy storage materials for coupled solar batteries, Acc. Chem. Res. 57 (2024) 1736–1746, https://doi.org/10.1021/ACS.ACCOUNTS.4C00222.

[14] W. Wang, X. Zhang, J. Lin, L. Zhu, E. Zhou, Y. Feng, D. Yuan, Y. Wang, A photoresponsive battery based on a redox-coupled covalent-organic-framework hybrid photoelectrochemical cathode, Angew. Chem. Int. Ed. 61 (2022) e202214816, https://doi.org/10.1002/ANIE.202214816.

[15] L. Jiao, X. Zhang, Y. Feng, J. Lin, D. Yuan, Y. Wang, Coupled solar battery with 6.9 % efficiency, Angew. Chem. Int. Ed. 62 (2023) e202306506, https://doi.org/10.1002/ANIE.202306506.
[16] D. Bae, G. Kanellos, K. Wedege, E. Drá, A. Bentien, W.A. Smith, Tailored energy level alignment at MoO_X/GaP interface for solar-driven redox flow battery application, J. Chem. Phys. 152 (2020), https://doi.org/10.1063/1.5136252/956823.
[17] K. Wedege, D. Bae, W.A. Smith, A. Mendes, A. Bentien, Solar redox flow batteries with organic redox couples in aqueous electrolytes: a minireview, J. Phys. Chem. C 122 (2018) 25729–25740, https://doi.org/10.1021/acs.jpcc.8b04914.
[18] D. Bae, G.M. Faasse, W.A. Smith, Hidden figures of Photo-charging: a Thermo-electrochemical approach for solar-rechargeable redox flow cell system, Sustain. Energy Fuels 4 (2020) 2650–2655, https://doi.org/10.1039/D0SE00348D.
[19] J. Kim, Imbalance of active ions through segmented electrodes: mass transfer characteristics of vanadium redox flow batteries, Sustainable Materials and Technologies 36 (2023), https://doi.org/10.1016/j.susmat.2023.e00637.
[20] J. Kim, H. Park, Recent advances in porous electrodes for vanadium redox flow batteries in grid-scale energy storage systems : a mass transfer perspective, J. Power Sources 545 (2022) 231904, https://doi.org/10.1016/j.jpowsour.2022.231904.
[21] L. Tang, P. Leung, M.R. Mohamed, Q. Xu, S. Dai, X. Zhu, C. Flox, A.A. Shah, Q. Liao, Capital cost evaluation of conventional and emerging redox flow batteries for grid storage applications, Electrochim. Acta 437 (2023) 141460, https://doi.org/10.1016/J.ELECTACTA.2022.141460.
[22] R. Chen, Z. Huang, R. Hempelmann, D. Henkensmeier, S. Kim, Vanadium redox flow batteries, in: Encyclopedia of Electrochemistry, Wiley, 2020, pp. 1–33, https://doi.org/10.1002/9783527610426.bard110010.
[23] N. Zheng, Q. Wang, X. Ding, H. Zhang, L. Duan, X. Wang, Y. Zhou, M. Sun, U. Desideri, Techno-economic analysis of a novel solar-based polygeneration system integrated with vanadium redox flow battery and thermal energy storage considering robust source-load response, Appl. Energy 376 (2024) 124288, https://doi.org/10.1016/J.APENERGY.2024.124288.
[24] N.M. Delgado, R. Monteiro, A. Mendes, The first approach to dynamic modeling of a solar vanadium redox flow cell, Nano Energy 89 (2021) 106372, https://doi.org/10.1016/J.NANOEN.2021.106372.
[25] G. Tian, R. Jervis, J. Briscoe, M. Titirici, A. Jorge Sobrido, Efficient harvesting and storage of solar energy of an all-vanadium solar redox flow battery with a MoS_2@TiO_2 photoelectrode, J. Mater. Chem. A Mater. 10 (2022) 10484–10492, https://doi.org/10.1039/D2TA00739H.
[26] J. Kim, H. Park, Experimental analysis of discharge characteristics in vanadium redox flow battery, Appl. Energy 206 (2017) 451–457, https://doi.org/10.1016/j.apenergy.2017.08.218.
[27] W. Lee, A. Permatasari, B.W. Kwon, Y. Kwon, Performance evaluation of aqueous organic redox flow battery using anthraquinone-2,7-disulfonic acid disodium salt and potassium iodide redox couple, Chem. Eng. J. 358 (2019) 1438–1445, https://doi.org/10.1016/J.CEJ.2018.10.159.
[28] K. Wedege, D. Bae, E. Dražević, A. Mendes, P.C.K. Vesborg, A. Bentien, Unbiased, complete solar charging of a neutral flow battery by a single Si photocathode, RSC Adv. 8 (2018) 6331–6340, https://doi.org/10.1039/c8ra00319j.
[29] D. Bae, G.M. Faasse, G. Kanellos, W.A. Smith, Unravelling the practical solar charging performance limits of redox flow battery based on the single photon device system, Sustain. Energy Fuels 3 (2019) 2399–2408, https://doi.org/10.1039/C9SE00333A.
[30] J. Wang, X. Liu, C. Lin, K. Zhang, K. Mei, Y. Yang, H. Shi, Z. Wang, Y. Zhang, S. Li, Dual photoelectrode-drived Fe–Br rechargeable flow battery for solar energy conversion and storage: a cost-effective approach, J. Power Sources 618 (2024) 235163, https://doi.org/10.1016/J.JPOWSOUR.2024.235163.
[31] S. Murcia-López, M. Chakraborty, N.M. Carretero, C. Flox, J.R. Morante, T. Andreu, Adaptation of Cu(In, Ga)Se_2 photovoltaics for full unbiased photocharge of integrated solar vanadium redox flow batteries, Sustain. Energy Fuels 4 (2020) 1135–1142, https://doi.org/10.1039/C9SE00949C.
[32] R. Yan, Q. Wang, R. Yan, Q. Wang, Redox-targeting-based flow batteries for large-scale energy storage, Adv. Mater. 30 (2018) 1802406, https://doi.org/10.1002/ADMA.201802406.
[33] K.S. Archana, S. Suresh, P. Ragupathy, M. Ulaganathan, Investigations on new Fe–Mn redox couple based aqueous redox flow battery, Electrochim. Acta 345 (2020) 136245, https://doi.org/10.1016/J.ELECTACTA.2020.136245.
[34] G. Jung, C. Moon, F. Martinho, Y. Jung, J. Chu, H. Park, A. Hajijafarassar, R. Nielsen, J. Schou, J. Park, P.C.K. Vesborg, O. Hansen, Y.S. Lee, S. Canulescu, B. Shin, Monolithically integrated $BiVO_4$/Si tandem devices enabling unbiased photoelectrochemical water splitting, Adv. Energy Mater. 13 (2023) 2301235, https://doi.org/10.1002/AENM.202301235.
[35] W. Li, J. Zheng, B. Hu, H.C. Fu, M. Hu, A. Veyssal, Y. Zhao, J.H. He, T.L. Liu, A. Ho-Baillie, S. Jin, High-performance solar flow battery powered by a perovskite/silicon tandem solar cell, Nat. Mater. 19 (2020) 1326–1331, https://doi.org/10.1038/s41563-020-0720-x.
[36] S.Y. Lee, P. Serafini, S. Masi, A.F. Gualdrón-Reyes, C.A. Mesa, J. Rodríguez-Pereira, S. Giménez, H.J. Lee, I. Mora-Seró, A perovskite photovoltaic Mini-Module-$CsPbBr_3$ photoelectrochemical cell tandem device for solar-driven degradation of organic compounds, ACS Energy Lett. 8 (2023) 4488–4495, https://doi.org/10.1021/ACSENERGYLETT.3C01361.
[37] K. Villa, J.R. Galán-Mascarós, N. López, E. Palomares, Photocatalytic water splitting: advantages and challenges, Sustain. Energy Fuels 5 (2021) 4560–4569, https://doi.org/10.1039/d1se00808k.
[38] L. Yan, D. Li, S. Li, Z. Xu, J. Dong, W. Jing, W. Xing, Balancing osmotic pressure of electrolytes for nanoporous membrane vanadium redox flow battery with a draw solute, ACS Appl. Mater. Interfaces 8 (2016) 35289–35297, https://doi.org/10.1021/ACSAMI.6B12068.
[39] W. Duan, A. Lambertz, K. Bittkau, D. Qiu, K. Qiu, U. Rau, K. Ding, A route towards high-efficiency silicon heterojunction solar cells, Prog. Photovoltaics Res. Appl. 30 (2022) 384–392, https://doi.org/10.1002/PIP.3493.
[40] J. Yu, P.S. Leonard, D. Qiu, Y. Zhao, A. Lambertz, C. Zahren, L. Volker, W. Duan, J. Yu, K. Ding, Light-induced performance of SHJ solar modules under 2000 h illumination, Sol. Energy Mater. Sol. Cell. 235 (2022) 111459, https://doi.org/10.1016/J.SOLMAT.2021.111459.
[41] G. Choi, P. Sullivan, X.L. Lv, W. Li, K. Lee, H. Kong, S. Gessler, J.R. Schmidt, D. Feng, Soft–hard zwitterionic additives for aqueous halide flow batteries, Nature 635 (8037 635) (2024) 89–95, https://doi.org/10.1038/s41586-024-08079-4.
[42] J. Li, Z. Xu, M. Wu, Halogen enabled aqueous flow cells for large-scale energy storage: current status and perspectives, J. Power Sources 581 (2023) 233477, https://doi.org/10.1016/J.JPOWSOUR.2023.233477.
[43] B. Bennett, J. Chang, A.J. Bard, Mechanism of the Br −/Br 2 redox reaction on platinum and glassy carbon electrodes in nitrobenzene by cyclic voltammetry, Electrochim. Acta 219 (2016) 1–9, https://doi.org/10.1016/j.electacta.2016.09.129.
[44] Z. Pei, Z. Zhu, D. Sun, J. Cai, A. Mosallanezhad, M. Chen, G. Wang, Review of the I^-/I_3^- redox chemistry in Zn-iodine redox flow batteries, Mater. Res. Bull. 141 (2021) 111347, https://doi.org/10.1016/J.MATERRESBULL.2021.111347.
[45] Y. Xu, C. Xie, T. Li, X. Li, A high energy density bromine-based flow battery with two-electron transfer, ACS Energy Lett. 7 (2022) 1034–1039, https://doi.org/10.1021/ACSENERGYLETT.1C02798.
[46] N. Elgrishi, K.J. Rountree, B.D. McCarthy, E.S. Rountree, T.T. Eisenhart, J. L. Dempsey, A practical beginner's guide to cyclic voltammetry, J. Chem. Educ. 95 (2018) 197–206, https://doi.org/10.1021/acs.jchemed.7b00361.
[47] W. Li, H.-C. Fu, L. Li, M. Cabán-Acevedo, J.-H. He, S. Jin, Integrated photoelectrochemical solar energy conversion and organic redox flow battery devices, Angew. Chem. 128 (2016) 13298–13302, https://doi.org/10.1002/ANGE.201606986.
[48] B.H. Robb, S.E. Waters, J.D. Saraidaridis, M.P. Marshak, Realized potential as neutral pH flow batteries achieve high power densities, Cell Rep Phys Sci 3 (2022), https://doi.org/10.1016/j.xcrp.2022.101118.
[49] Z.J. Yu, J.V. Carpenter, Z.C. Holman, Techno-economic viability of silicon-based tandem photovoltaic modules in the United States, Nat. Energy 3 (9) (2018) 747–753, https://doi.org/10.1038/s41560-018-0201-5.
[50] J. Li, Q. Wang, J. Zhang, Design and development of large-scale vanadium redox flow batteries for engineering applications, J. Power Sources 591 (2024) 233855, https://doi.org/10.1016/J.JPOWSOUR.2023.233855.